EMT Conversion of Composite Broadband Absorbent Metamaterials for Stealth Application Over X-Bands

JUNPING DUAN [1], RUI LIU[1], HONGCHENG XU[2], RUI ZHANG[1], BINZHEN ZHANG[1], AND BYUNG-SUNG KIM[3], (Member, IEEE)

[1]Key Laboratory of Instrumentation Science and Dynamic Measurement, Ministry of Education, North University of China, Taiyuan 030051, China
[2]School of Mechano-Electronic Engineering, Xidian University, Xi'an 710071, China
[3]College of Information and Communication Engineering, Sungkyunkwan University, Suwon 440-746, South Korea

Corresponding authors: Binzhen Zhang (zhangbinzhen@nuc.edu.cn) and Byung-Sung Kim (bskimice@skku.edu)

ABSTRACT A validating approach for electromagnetic thermal (EMT) conversion of a composite broadband absorbent metamaterials (AMs) is proposed in this paper. The integrated multilayer AMs consisting of top square loop (Q-loops) array layer, middle metal plate-polymer sandwich, bottom Q-loops array layer stacked vertically is analyzed with finite-different time-domain (FDTD) algorithm and fabricated by High Density Interconnector (HDI) process and Micro-electromechanical Systems (MEMS) technology. The implemented composite layered structure with the dielectrics and subsequent multi metal loops has broadband bandwidth over 2.5GHz in X-bands. High absorption performance in various incident waves with different polarizations and incident angles basically maintains a fixed efficient level of the AMs with diverse absorbing states in wide operating band. Electromagnetics and thermal multiphysics analysis validates the EMT conversion of the AMs in induced strong electromagnetic resonance. The integrated thermal conduction device is loaded on the back of AMs to transfer the converted thermal energy in time, which effectively reduces the surface thermal distribution. Finally, absorbent properties tested by free space methods and thermocouple and infrared thermal imaging (ITI) system shows the polarization independent energy transformation in greatly accordance with numerical analysis. This investigation shows the potential application of AMs in stealth systems to achieve both electromagnetic stealth and infrared thermal stealth through EMT energy conversion.

INDEX TERMS Broadband, absorbent metamaterials (AMs), electromagnetic thermal (EMT) conversion, stealth, thermoelectricity.

I. INTRODUCTION

Artificial metamaterials, which own advantaged electromagnetic (EM) manipulating capability in dual negative refractive index modification [1], [2], radar cross-section (RCS) reduction [3], [4], frequency selectivity [5]–[8] and antenna properties improvement [9], [10], have intrigued great interests for stealth domain [11], [12], super-resolution imaging [13]–[15], energy harvesting [16]–[19], beam scanning [20], [21], and even acoustical [22]–[24], terahertz [25],

optical [26]–[28] applications. EM manipulation means the efficient energy transfer or property transformation of absorbent metamaterials (AMs). Harvesting energy or special property research was conducted with various AM structure by many scholars. However, the application and conversion mechanism of AMs in the EM energy control lacks definite and more profound investigation. Energy conversion study using metamaterials is of a sluggish development to achieve commercial application.

The EM energy harvesting strategy using AMs is mainly undergone by available absorbing source spectrum of meta-structure and the absorbing energy development

The associate editor coordinating the review of this manuscript and approving it for publication was Kuang Zhang.

attributes to metal LC resonance [29], surface resonance [30], ohmic loss [31], dielectric loss [32], and wave propagated paths loss [33], [34]. Most of them dynamically produce a valid constraint of receiving wave in the AMs interior and are absent of energy conversion verification by harvesting EM wave. For examples, [35]–[40] proposed broadband or dual-band metamaterial absorber applied to solar cells while these studies only focused on high absorbing. Since most of the incident electromagnetic energy is transformed into thermal distribution through the loss of AMs, the full analysis of energy harvesting mechanism is significant to investigate the electromagnetic thermal (EMT) conversion. Additionally, most target detection radar signal bands are concentrated in the X-band, so the military targets must manipulate the incident waves to achieve stealth. In general, active stealth for evading radars can be achieved by loading AMs to absorb and manipulate scattered waves [41]–[45]. But at the same time, the large amount of thermal energy generated by electromagnetic energy conversion will cause the surface temperature of the target to rise sharply, which is very unfavorable to infrared thermal stealth. The existing research results only consider the electromagnetic stealth of the weapon system, and ignore the infrared thermal stealth demand generated by the converted thermal energy. Therefore, the investigation on the electromagnetic energy conversion of X-band ultra-wideband AMs is crucial to the development of stealth applications of AMs.

In this study, a composite multilayer broadband absorbent metamaterial harvesting induced EMT conversion was investigated, which provides a solution to the above problems. It can be loaded in stealth system to achieve the electromagnetic stealth effect while transmitting the converted thermal energy in a timely manner through a rear heat transfer device. The proposed AMs consist of multi-layer substrate, multi Q-loops array, and metal plate spatial distribution vertically and entire construction of structure is fabricated by High Density Interconnector (HDI) process in top and bottom Q-loops layer, and by Micro-electromechanical Systems (MEMS) technology in multi-layer assemble integration. The back of AMs is loaded with integrated thermal devices. The finite-different time-domain (FDTD) algorithm simulating the virtual mode is connected with the free space methods in EM properties test to verify the validity of the proposed AMs. Finally, Multi-physics field analysis and thermal measurements validate the EMT conversion with potential applications in EM energy conversion and stealth systems.

II. METHODS AND RESULTS
A. THEORETICAL BACKGROUND
Electromagnetic AMs consisting of infinite cells with periodical arrangement consistently induce organized LC, dielectric surface and dipole resonance what restrain EM wave propagation in a resonant tank leading valid loss of EM energy. When both the equivalent permittivity $\varepsilon_e = \varepsilon' - j\varepsilon''$ and permeability $\mu_e = \mu' - j\mu''$ of AMs are equal to the acute

degree of motion of EM wave with incidence to materials in vacuum, EM wave propagates over an AMs achieving perfect impedance matching. ε' is a parameter that describes the degree of polarization, and μ' describes the degree of magnetization. ε'' and μ'' denotes the electronic and magnetic loss of measured materials respectively [42], which configurates the absorbent level of the AMs evaluating the absorptivity. As to a planar AMs structure containing special metal resonant elements, the formula $A(w) = 1 - R(w) - T(\omega) = 1 - |S_{11}|^2 - |S_{21}|^2$ can represent the theorical absorptivity, where $R(w) = |S_{11}|^2$ is reflectivity and $T(\omega) = |S_{21}|^2$ is transmittivity. Due to one special metal element corresponding to a solid electric resonance, the physical AMs can be severed as frequency selective surface (FSS) with precise working frequency. Precise manipulation via the FSS input impedance $Z(w) = \sqrt{\mu(w)/\varepsilon(w)}$ is necessary to enhance absorptivity. Furthermore, many factors like resonant elements, materials, dimension, and incident wave totally modulate $Z(w)$ to effective AM properties. Hence, $R(w)$ can be calculated as formula (1)

$$R(w) = |S_{11}|^2 = \left(\frac{Z(w)-1}{Z(w)+1}\right)^2$$
$$= \frac{[(Re\{Z(w)\} - Z_0 cos\theta)]^2 + [Im\{Z(w)\}]^2}{[(Re\{Z(w)\} + Z_0 cos\theta)]^2 + [Im\{Z(w)\}]^2}, \quad (1)$$

where $Z_0 = 337\Omega$ is the wave impedance of incident wave in free space, θ is the incident angle of EM wave. Hence, the reflectivity becomes zero for the normalized complex impedance near 1. Moreover, the equivalent refractive index $n_e = n' - jn''$ of AMs is the major parameter resolving the transmittivity as formula (2)

$$S_{21}^{-1} = \left[\sin(n_e kd)\frac{i}{2}\left[Z(w) + \frac{1}{Z(w)}\right]\cos(n_e kd)\right]e^{ikd}, \quad (2)$$

where $k = \omega/c$ is the free wave number, the thickness of meta-surface is d. Then, $S_{21}^{-1} = e^{-1(n'-1)}e^{n''kd}$ when the impedance of AMs is matched to free space and the normalized complex impedance equates to 1, $T(\omega) = |S_{21}|^2 = e^{-n''kd}$ [43]. Therefore, no transmitted EM wave penetrates AM with infinite n''. Above all, two main factors can manage the perfect absorptivity if the modulation of them is suitable for the microstructure, arrangement and selective substrate.

Since the equivalent permittivity and permeability of AMs cannot be simulated and measured directly, when the result of the S parameters is obtained, the equivalent permittivity and permeability can be extracted through the S parameters [46], [47]. In fact, the backplane of AM is usually a metal film whose thickness is greater than the skin depth of the EM wave at the operating wavelength, so no the transmitted wave will penetrate. Without involving S_{21}, the equivalent permittivity ε_e and permeability μ_e can be obtained from
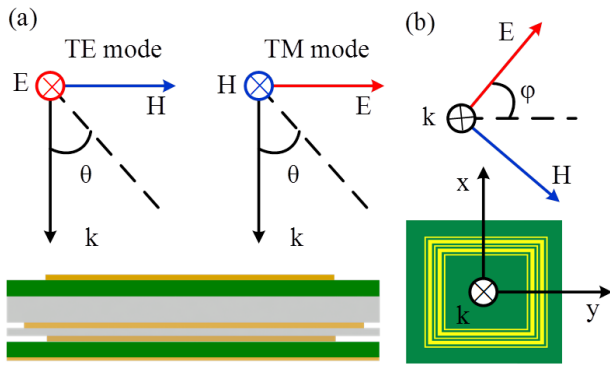
FIGURE 1. Configuration of the incident EM wave to AMs: (a) TE and TM mode of oblique incident wave; (b) polarization mode of vertical incident wave.

FIGURE 2. Multi-layer composite metamaterial elements diagram. (a) 3D model space pattern showing resonant multi-square loop and middle patch and various insulator substrate layers; (b) top planform detail of the five square loops array; (c) detail drawing of the metal Q-loop.

equation (3)

$$\chi_{es} = \frac{2j}{k} \frac{S_{11} - 1}{S_{11} + 1}$$

$$\chi_{ms} = \frac{2j}{k} \frac{S_{11} + 1}{S_{11} - 1}$$

$$\varepsilon_e = 1 + \frac{\chi_{es}}{d}$$

$$\mu_e = 1 + \frac{\chi_{ms}}{d}, \tag{3}$$

where χ_{es} and χ_{ms} are the electric susceptibility and magnetic susceptibility, respectively. Therefore, the absorbent level of AMs to EM wave can be evaluated according to the degree of polarization and magnetization.

Efficient EM energy consumption in overall AMs primarily stands for EM wave absorption. Temperature change from thermal storage in multilayer meta-surface induced resonance can be of a precise index to represent the absorbing level of incident wave as formula (4)

$$\Delta T = \frac{Q_{abs}}{m \cdot C_e} = \frac{Q_{abs}}{\sum V_i \rho_i c_i}, \tag{4}$$

where Q_{abs} is the absorbed energy from incident wave by AMs, m is the total mass of material, and C_e is the equivalent specific heat capacity. As to multilayer composite materials, the mass storage heat can be characterized by the volume V_i, density ρ_i, and specific heat capacity c_i of composing each thin film. Hence, thermal performance in consuming EM energy attributes to absorbing wave energy and specific heat level.

Structural properties of AMs can be reflected to EM response with the incident wave-transformation. Therefore, the different oblique and polarized incident waves transmit to the resonant construction in different mode, which must be verified adequately. Fig.1 shows the illustration of oblique incident waves of different polarization in terms of the physically arranged AMs. Transverse electric (TE) and transverse magnetic (TM) wave are vertically incident on the surface of AMs as shown in Fig.1. (a) and the electric and magnetic direction of oblique incident wave parallels with the surface.
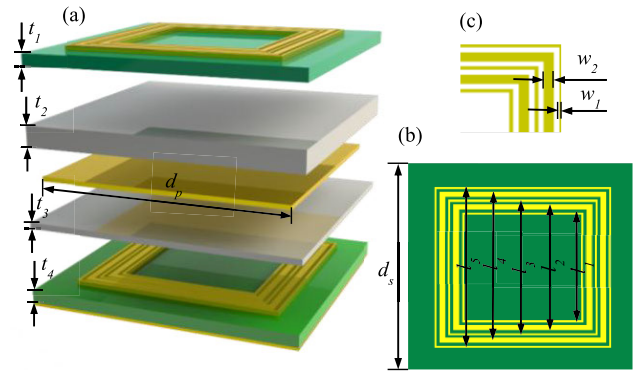
The wave vector K of the polarization wave is vertical to AMs as shown in Fig.1. (b). Both plots give a clear representation of the incidence angle θ and the polarization angle φ.

B. IMPLEMENTED METHODS

Entire verification from numerical implementation to accurate fabrication, and finally experimental execution is of sophisticated processing to verify the validity of the proposed strategy. The implemented methods mainly include three scientific process, full-wave electromagnetic simulation, multiple structural manufacture, and physical measurement.

1) FULL-WAVE SIMULATION FOUNDATION AND NUMERICAL MODELING

Numerical EM calculation by means of the finite-different time-domain (FDTD) method packaged in commercial full wave analysis software, Computer Simulation Technology (CST), is conducted to an infinite planar array composed of uniform cells with periodical configuration. Based on FDTD algorithm, floquet boundary and excitation conditions are also managed to become a linear periodical working in isolation, which generates the representation of the metamaterial planar array out of one cell.

As shown in Fig.2.(a), detailed cell structure comprises backside solid copper ($\sigma = 5.88e + 07S/m$) foil layer, insulator layer of Rogers 5880 (Ro5880, $\varepsilon = 2.2$, $\tan\delta = 0.0009 * (1 + T/300\,[K])$), five metal resonant Q-loop array, flexible adhesive layer of Polydimethylsiloxane (PDMS, $\varepsilon = 2.75$, $\tan\delta = 0.03 * (1 + T/300\,[K])$), sputtered aluminium (Al, $\sigma = 3.56e + 07S/m$) plate layer, PDMS layer, Flame Retardant 4 (FR4, $\varepsilon = 4.4$, $\tan\delta = 0.02 * (1 + T/300\,[K])$), and Q-loops array layer from the bottom to the top. The spacing location and dimension of two Q-loops maintain counterpart in the dielectric plate and the wire width of five Q-loops array is periodic in the sequence of between two sizes as shown in Fig.2. (b) and (c). The developed dimensions of each part are shown in Table. 1.
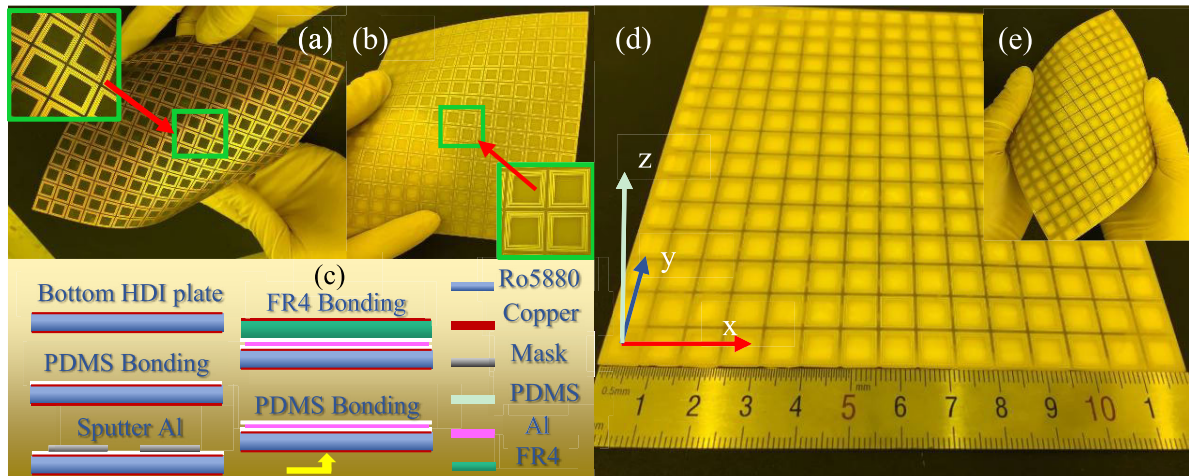
FIGURE 3. Fabricated physical prototype and manufacturing process. (a) and (b) bottom and top flexible plates based on the HDI processing fabrication, respectively. (c) final prototype manufacturing process with bonding of various insulator substrate and sputtering of Al based MEMS technology, (d) final physical prototype, (e) illustration of the flexible AMs.

TABLE 1. Spacing detail dimensions of metamaterials cell.

Parameter	t_1	t_2	t_3	t_4	d_p	d_s
Value(mm)	0.254	0.4	0.4	0.254	7.37	8.0
l_1	l_2	l_3	l_4	l_5	w_1	w_2
6.2	6.03	5.61	5.44	5.02	0.15	0.4

2) MEMS AND HDI TECHNOLOGY BASED SAMPLE STORAGE FABRICATION

Metal Q-loops array on the top and bottom insulator substrate is constructed with the etching process by HDI technology owing to the scale of the Q-loops array on the order of microns, as shown in Fig.3. (a) and (b). Q-loops etching thickness is 17μm. The bonding process between top and bottom dielectrics is conducted with two flexible adhesive PDMS-layers which shows high elasticity and tensile properties. PMDS is configured with the SYLGARD 184 and fixation mixed in 10:1 mass ratio. Middle reflective Al metal foil layer with the thickness of 500nm is ejected in PDMS by magnetron sputtering machine. As shown in Fig.3. (c), multi-layer integration between different dielectrics is realized by cationic bonding technology, and ultra-thin Al-foil is sputtered on the still PDMS plate with the aid of magnetron sputtering machine for 3 hours. The sample storage is fabricated by the above MEMS technology as shown in Fig.3. (d). Overall prototype consists of 15×15 cells of metamaterials elements and its area is $12 \times 12 \text{cm}^2$.

3) ABSORPTION SPACE TEST AND THERMAL FIELDS MEASUREMENT

Free space test method, as shown in Fig.4. (a) and (c), is applied to achieve the absorbing features by transmitting a standard TE or TM beam from the horn antenna to the AM sample vertically. TE or TM mode is excited when the short edge or the long edge of the horn antenna is vertically aligned to the ground, respectively. By modifying the position of the turntable of the horn antenna and rotating the sample supporting platform, respectively, the response of absorptivity to AMs for different polarizations and incident angels are measured. A network analyzer formulates the field spectrum in the Fourier transform to obtain absorptivity.

Moreover, detail of thermal fields monitor (TFM) system is shown as Fig.4. (b). An ITI camera monitors the tested AMs in the EM incident circumstance. Through EM wave stimulating the ohmic loss and dielectric loss of AMs, the transformed thermal distribution can be obtained by the TFM in short time. The initial temperature of the testing component is held at a constant temperature of the 293K (20°) to reduce the disturbance from external environment condition.

C. VERIFICATION RESULTS ANALYSIS

1) S-PARAMETER CHARACTERISTICS AND VALID ABSORPTION

The definite absorbent property of an artificial metamaterial must be verified by multi factor-analyses, such as co-polarization and cross-polarization, TE and TM incident wave and others. When normal TE incident wave propagates the AM surface, the reflective coefficients of co-polarization and cross-polarization are shown in Fig.5. (a). It is obvious that two powerful resonances occur at the frequency of 8GHz and 10 GHz, and the co-polarized reflective coefficients below -8dB can be obtained in the range of 7.8~10.3GHz. By contrast, the cross-polarized reflective coefficients level is below -20dB, which indicates the weak transformation performance of the incident wave from the co-polarization to the cross-polarization. The transmittivity of AMs is about zero due to the shield function of the back plate. Also, the transformed intensity (720°) of the cross-polarized reflective phase is obviously more than the co-polarized ($-104°$ ~69°)
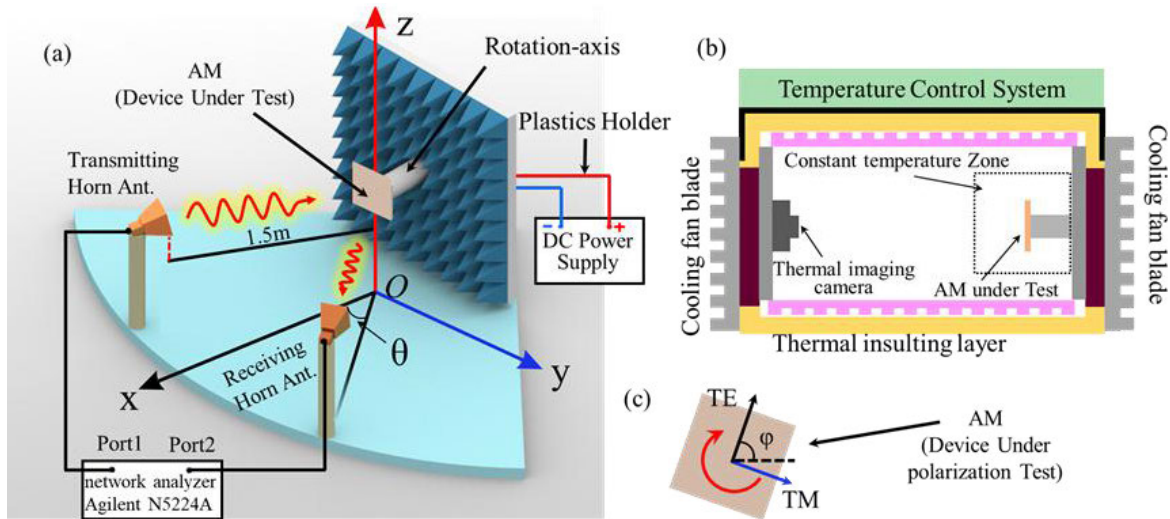
FIGURE 4. EM and thermal characteristic measurement of AMs (a) free space test to AMs in different oblique incident wave; (b) real time thermal imaging monitor system; (c) test realization in different polarization incident configuration.
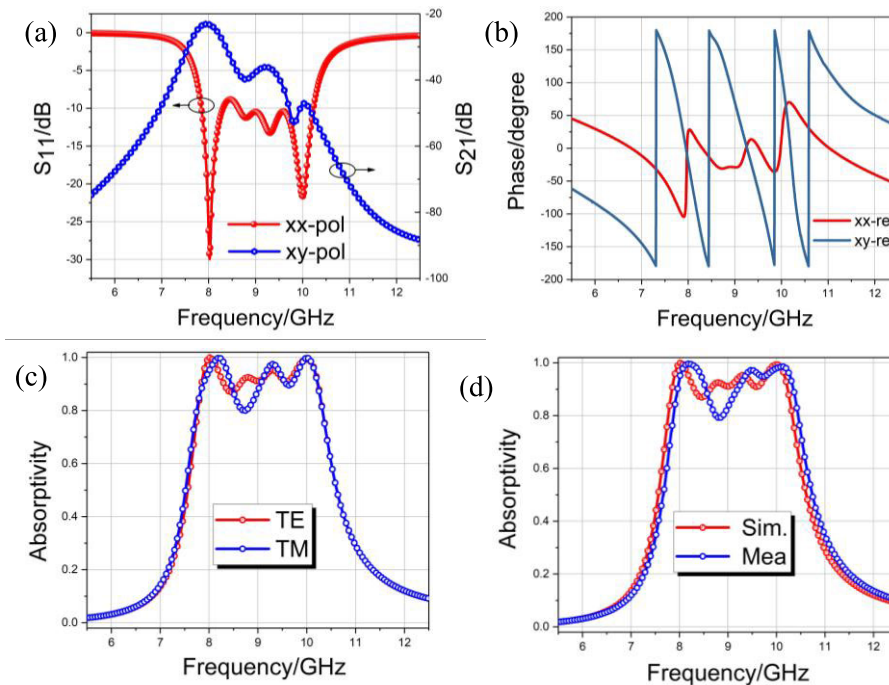

FIGURE 5. Virtual and physical EM responded spectra of the AMs (a) reflective coefficients of the co-polarization and cross-polarization in TE incident wave; (b) reflective phase of the two polarization modes; (c) normalized numerical absorbent spectra of the AMs in TE and TM incident wave; (d) simulated and measured absorptivity of the AMs in TE mode.

and the strongest changes of the phase in co-polarization mostly occurs at the endpoint of the working band as shown in Fig.5. (b). This longer delay of the reflected phase in cross-polarization exhibits little returned EM wave to out-put port, which further verify occurs in AMs with the definite absorption instead of polarized transformation.

The absorptivity of AM is shown in Fig.5. (c) when transverse electric magnetic wave is normally incident on

the meta-surface. The absorption in TE and TM incident wave almost maintains uniformly and only little discrepancy is observed at 8.8GHz as the electric dipole absorption of AM is stronger than the magnetic. The bandwidth of valid absorption over 70% nearly achieves 2.7GHz (7.7~10.4GHz). Fig.5. (d) shows simulated and measured absorptivity of AMs in TE mode and the measured absorbent bandwidth (BW) is 2.73GHz (7.8~10.53GHz).
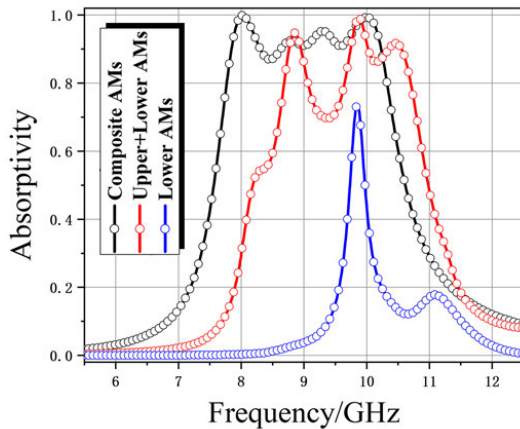
FIGURE 6. Simulated absorptivity of the lower AMs, upper + lower AMs, and composite AMs, respectively.

FIGURE 7. E-field distributions of AMs at 8GHz, 9GHz, and 10GHz, respectively (a)~(c) E-field profile in the strongest position of the AM; (d)~(f) top view of E-field distributions of the AMs.

FIGURE 8. Current distributions of AMs at 8GHz, 9GHz, and 10GHz, respectively (a)~(c) slot's current vector flow of the AMs; (d)~(f) detailed flow direction of each slot's rampart corresponding to the current vector at different frequency.

This broadband response attributes to the well-designed multiple resonances of Q-loops of the proposed AM cell and structural composite layer with the stronger dielectric loss. Furthermore, the feature of broadband complies with the ultra-wideband principle [41] which can be formulated as BW = $\left(f_{max(abs \geq 0.7)} - f_{min(abs \geq 0.7)}\right)/f_c > 25\%$ (f_c is the center frequency of working band.) and the actual BW level of the proposed AMs equals to 30% here.

2) MULTILAYER STRUCTURE DESIGN MECHANISM ANALYSIS

Due to the design of the AMs structure determines its absorption properties, the Q-loops array and the structural composite layer with high dielectric loss make the proposed AMs have multiple resonances, thereby achieving broadband. At the beginning of the design, a single-structure AMs that used an insulating dielectric layer Ro5880 to separate the top Q-loops array and the metal backplane (copper) is simulated by CST, as shown in Figure 6. It can be found that the absorptivity is low and the bandwidth is narrow. Therefore, we propose to superimpose another AMs with the same Q-loops array on the top of the single-structure AMs. It is worth noting that the metal back plate of the upper superimposed AMs is in the middle of the multilayer structure, it not only needs to feed back part of the incident wave to the first Q-loops array layer to loss, but also transmits part of the incident wave to the second Q-loops array layer to consume. For this reason, the metal back plate is selected to be aluminum plate with sputtered thickness of only 500 nm. The use of aluminum as the intermediate metal back plate also benefits from its better ductility, which prevents micro-cracks after multiple bending in the middle. In addition, considering that the temperature of the upper superimposed AMs increases rapidly with electromagnetic incidence, the material of the dielectric layer of the upper AMs is FR4 with good flame retardant properties. After superimposing the upper AMs, it can be found that the composite structure significantly increases the absorptivity and broadens the bandwidth. Finally, the flexible adhesive layer PDMS is used to bond the upper and lower
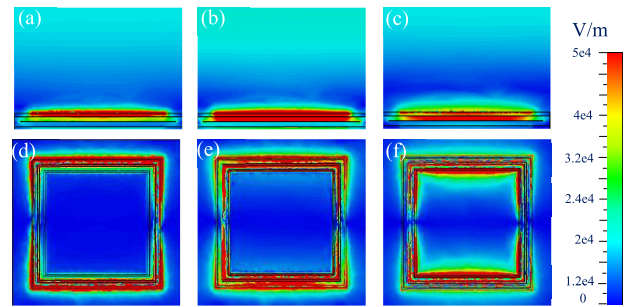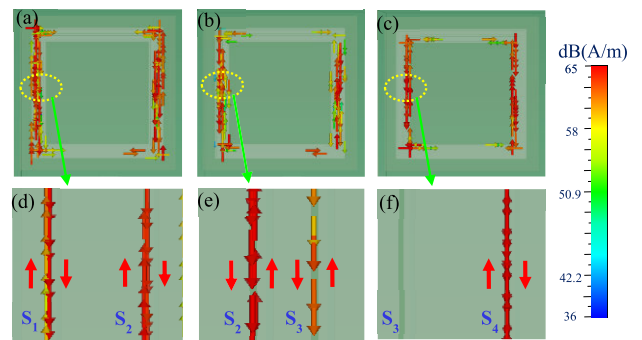
single-structure AMs together to form a composite multilayer structure AMs, so that the absorptivity in the whole frequency range is greater than 85%.

3) BROADBAND IMPLEMENTED VIA ELECTRIC PROPERTIES

Electric properties representations which are shown as the E-field distributions in Fig.7 and detailed current vector flow in Fig.8 are of significant to verify broadband implementation derived from complex resonance. The E-field distributed profiles in the strongest position of the proposed AMs in TE mode are shown in Fig.7. (a)~(c) versus 8GHz, 9GHz, and 10GHz, and the fierce electric configuration presents a downtrend from the position of the superficial Q-loops, to superficial Q-loops and upper FR4 layer, to merely upper FR4 with increasing frequency. Four slots between different Q-loops are defined as $S_1 \sim S_4$ from the outer to inner loop. According to superficial E-field distribution as shown in Fig.7. (d)~(f), strong resonant location gradually deviates from outer to inner loops, which bears out the negative correlation between the electric resonant path circumference and the working frequency. The low-frequency resonant response majorly occurs around S_1 and S_2, middle resonant response around S_2 and S_3, and high resonant response around S_4. Little electric flow is distributed in the adjacent Q-loops of the slot. The physical structural arrangement of sequential
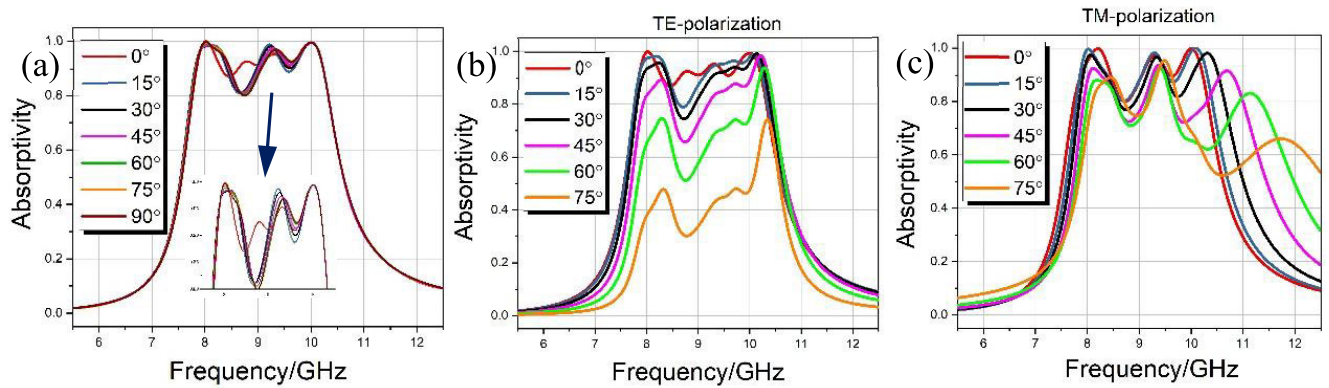
FIGURE 9. Numerical polarization properties of the AM in different working mode (a) absorbance under the normalized incident polarized wave with different angles; (b) and (c) absorbance characterization under oblique incident wave in TE-polarization and TM-polarization mode, respectively.

metal and corresponding the extended depth of the dielectric resonant location facilitate the forming of ultra-wideband absorbent.

Higher broadband absorption attributes to the successive resonances derived from slot's EM functioned position of which circular currents flow along the rampart. The current vectors create an obvious dipole resonance, as shown in Fig.8. (a)~(c), at the three operating frequencies, respectively. The directions of these vectors flow are vertical to the above E-field distributed profile in accordance with the forming reason of E-fields. The current details are shown in Fig.8. (d)~(f), which present the corresponding resonant location between the superficial currents and E-fields. The rampart current of each slot flows reversely at different frequency, which indicates the dipole resonances in each slot is excited to manipulate the EM resonant absorption.

4) AMS POLARIZATION CORRELATION

Polarization feature of AMs is a key indicator to evaluate the tolerance that decides the full-wave configuration between the incident wave deflection and EM function of AMs. Fig.9. (a) shows the absorptivity of AMs under the normalized incident TE (TM) polarized wave with different angles. The obvious polarization independent with the changes of polarized angle is of a representation which exhibits the favorable absorbance in full azimuthal polarized rotation incident wave. Little variation of the absorptivity attributes to the convergence level of different simulated software. The TE mode is less absorbed with the increase of the incident angle. However, the absorptivity over 60% is still achieved in working band when $\theta < 50°$ as shown in Fig.9. (b). Although the absorbent peak in high frequency is right-shifted and decreases with the increase of θ for TM mode, the excellent EM-wave absorbing over 70% maintains in low frequency when $\theta < 75°$ as shown in Fig.9. (c). The absorbent responses in both incident modes basically keep a high level in the wide incident angles, which validates the polarization insensitivity of the proposed AMs adequately. As the AMs absorbing
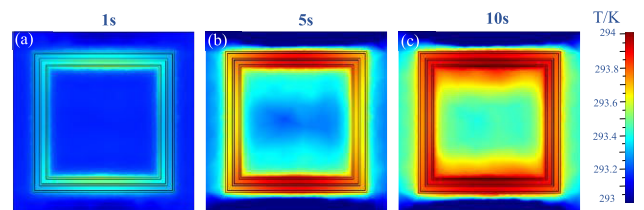

FIGURE 10. Superficial thermal distribution of the AM in the radiation of the standard vertical incident EM wave at different time (a) 1s; (b) 5s; (c) 10s.

belongs to electric dipole resonant function, the absorbent effects in the TE mode perform stronger than the TM mode.

D. EMT CONVERSION

Standard TE wave with the incident power of 1W at the center frequency (f_c) vertically propagates to the proposed AMs surface activating the ohmic and dielectric losses which generate complex thermal distributions in metal and dielectric portion. The resonant-thermal multiphysics simulation in a short time (ten seconds) aims to avoid the loss of the energy from EMT which is manipulated by the simulation with the aid of the commercial software CST. Fig.10 shows the superficial thermal distribution of the proposed AMs in the radiation of the standard vertical incident EM wave at different time. The apparent thermal field magnitude gradually becomes stronger from 1s to 10s, and the thermal energy focuses on the two flanks of the different Q-loops. High frequency activates the inner loops resonance where the initial thermal field is produced as shown in Fig.10. (a). Thermal diffusion is generated to other loops and dielectric surface as shown in Fig.10. (b) and (c) with the time going. These energy transformation from the full wave simulation validates the certain EMT mechanism.

Temperature responded variation of the proposed AMs in EM incident circumstance at 9.5GHz with the time is illustrated in Fig.11. The logarithmic count methods efficiently characterize the minute level of temperature variation (DT). The dynamic response of DT is timely modified
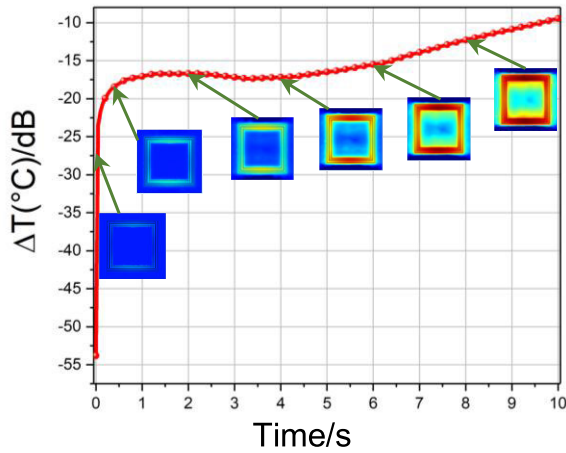
FIGURE 11. Evolution of temperature response in EM incident circumstance at 9.5GHz with the time.

FIGURE 12. The photograph of the experimental setup and prototype (a) free space test platform; (b) thermocouple (UT320D); (c) ITI camera (FLIR ONE) and (d) the AMs loaded with the integrated thermal conduction device.

at the range of $-54 \sim -9$dB. The initial fast enhancement of DT corresponds to the inner Q-loops resonance and the gradual increment of DT corresponds to the thermal diffusion accumulation. It can be found in the thermal transformation that EMT mechanism with a wide dynamic response is operated via harvesting EM energy of metamaterials absorbent behaviors.

E. EXPERIMENTAL ANALYSIS AND VERIFICATION

The fabricated physical prototype is measured by free space test platform as shown in Fig.12. (a). The introduction of the space test methods can measure the polarization and oblique propagation properties as shown in Fig.13. The physical polarization sensitivity of the fabricated AMs is illustrated in Fig.13. (a). The bandwidth of the measured absorptivity over 80% is about 2.6GHz and it produces no absorbent fluctuation with the polarization angle variation ($0° \sim 45°$), which is of in great agreement with the numerical data. Additionally, the absorptivity of proposed AMs in standard TE and TM oblique incident wave with different angles is tested and Fig.13. (b) and (c) exhibit the absorbent
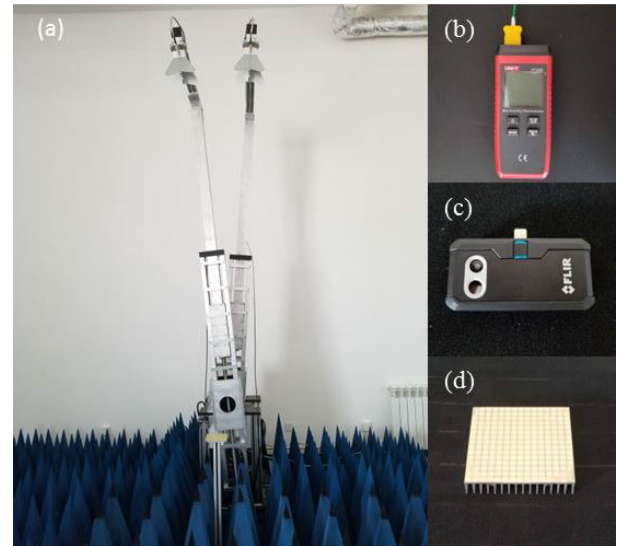
response, respectively. The absorptivity in TE mode performs over 63.3% in the frequency bandwidth of 2.85GHz (7.75$\sim$10.6GHz) and over 66.2% in the frequency bandwidth of 3.36GHz (7.84$\sim$11.2GHz) in TM mode when $\theta \leq 45°$. Only the frequency deviation of 600MHz represents in TM mode with oblique incident angle of 45°. The oblique incident measurements in two mode make identical trends with above simulated. Physical high absorptivity in various polarization and incident angles oblique incident wave validates that the proposed AMs possesses the insensitivity to EM wave. These advantaged properties show great potential in the actual complex energy conversion with wide incident angle range.

Moreover, the temperature responded variation of the designed AMs under the irradiation of the 9.5GHz incident EM was measured using a thermocouple (UT320D), as shown in Fig.14. With the increase of time, the measured temperature response curve agrees well with the simulation curve.
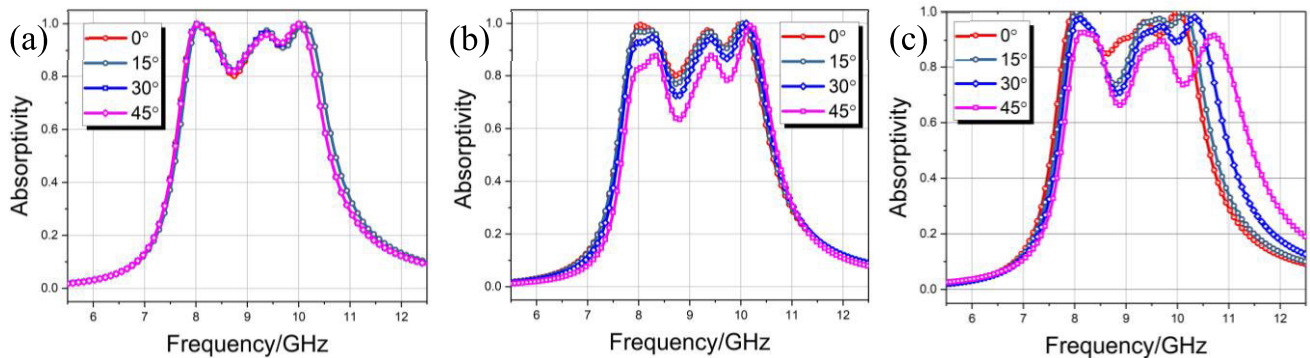

FIGURE 13. Physical polarization sensitive properties of the proposed AMs (a) measured absorptivity under the polarization incident wave with different angles; (b) and (c) measured absorptivity under oblique incident wave in TE-polarization and TM-polarization mode, respectively.

TABLE 2. Comparison between the AMs in this work and others.

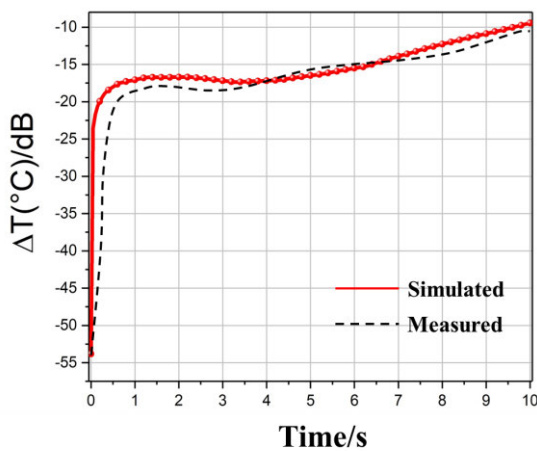| AMs	Center Frequency (GHz)	Number of Layers	Thickness (mm)	Flexibility	EMT Verification
[48]	8.9	3	1.6	No	No
[49]	10.8	3	3	No	No
[50]	10.1	25	5.45	No	No
[51]	11.36	3	2	No	No
[52]	6.95	4	6.55	No	No
[53]	10.2	1	3.2	No	No
This work	9.05	8	1.36	Yes	Yes

FIGURE 14. Measured temperature responded variation in EM incident circumstance at 9.5GHz with the time.

The ITI camera (FLIR ONE) plots superficial thermal distribution of the proposed AMs in the TFM system as shown in Fig.15, which verifies the electric-magnetic-thermal multi-physics simulation. More superficial thermal accumulation of the substrate illustrates the transfer from the self-absorbance to heat in the TFM zone when the incident time of EM wave is 10s. Major stronger thermal performance focus on the Q-loops indicates the availability of EMT conversion from the induced resonance. After the AMs were loaded with the integrated thermal conduction device, the surface thermal distribution showed a significant order of magnitude decrease,

almost equivalent to the thermal distribution without the EM incident, as shown in Fig.15. (d). This shows that AMs loaded with thermal conducting device can effectively reduce the surface thermal distribution and achieve good thermal stealth performance.

EMT conversion performance of the proposed AM shows the stronger electric resonance which validates the transfer of the incident EM energy to the thermal accumulation. As the construction of a stable TFM system costs too much and is disturbed from outer environment, the test time is short in terms of actual necessity. Therefore, the EMT verifications and the measurements in physical EM environment applied to various components with long time falls under the scope of future work.

Considering that the surface temperature of AMs increases rapidly when EM wave is incident under high power as well as the heat resistance of AMs in high-temperature environments, the influence of temperature change on AMs properties is discussed. In the structural composite layers composed of Q-loops array, metal plate and multilayer dielectric, the melting point of aluminum and copper is very high and the coefficient of thermal expansion is relatively low, which are 2.30×10^{-5}/K and 1.67×10^{-5}/K, respectively. However, the continuous temperature resistance of FR4 and PDMS is about 140 °C, and the Tg value of Ro5880 is relatively high. Therefore, the dielectric substrates are more sensitive to temperature increase.

In order to explore the change of AMs properties with increasing temperature, the fabricated prototype is placed on a temperature-adjustable thermostat (DXY-1010) with the
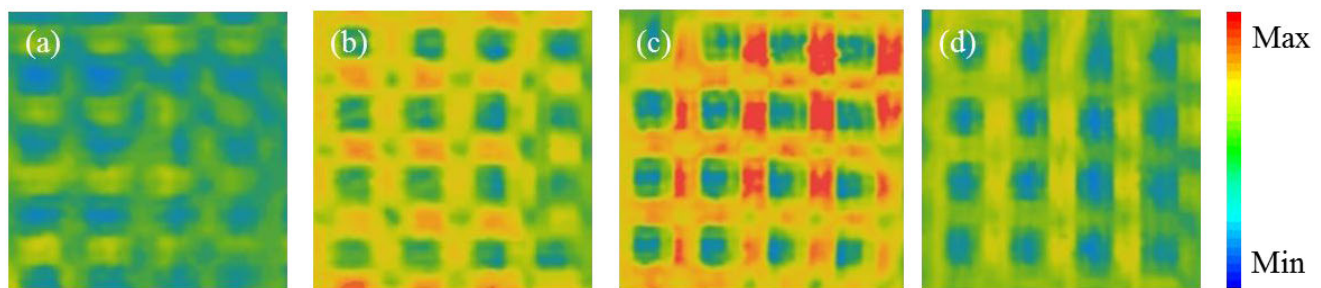

FIGURE 15. Superficial thermal distribution of the proposed AMs by the infrared thermal imaging camera in the radiation of the standard vertical incident EM wave of 9.5GHz at different time (a) 0s; (b) 5s; (c) 10s and (d) loaded conducting device.

same size ($12 \times 12cm^2$) as the sample, and then tested on the free space test platform. It can be found that when the temperature of the thermostat is lower than 105 °C, the absorptivity of the prototype is basically consistent with that under room temperature environment. When the temperature is higher than 105 °C, the prototype is thermally expanded as the temperature increases, the absorptivity significantly decreases as well as the EMT conversion capability is reduced. When the temperature reaches 120 °C, the multilayer structure begins to peel off and separate, and the performance of the AMs fails. This indicates that the proposed AMs has good heat resistance in a higher temperature range.

To better compare the number of layers, thickness and other properties of the proposed AMs, Table 2 lists the main features of some related works. It is worth noting that the proposed AMs has a minimum thickness and good flexibility. At the same time, multi-physics field analysis and thermal measurements validate the EMT conversion of AMs.

III. CONCLUSION

This study demonstrates an EMT conversion strategy of a composite active broadband AMs with high absorption and polarization insensitivity. The physical mode of the proposed AMs is constructed from the FDTD simulated structure to the fabricated sample storage by HDI and MEMS process. The structural configuration of the multi-layer composite features and sequential loops array arrangement of the proposed AMs enables to widen the bandwidth in X-bands. The verification for the various incident waves and infrared thermal imaging exhibits the polarization independent EMT conversion of the AMs at strong induced electric resonance. The ITI camera plots superficial thermal distribution of AMs after loading the integrated thermal conduction device, which shows that the thermal distribution on the surface of AMs can be effectively reduced. This investigation validates the EMT conversion of the proposed AMs to be further available to the thermoelectricity research of metamaterials and the research on AMs to realize both electromagnetic stealth and infrared thermal stealth is of great significance.

REFERENCES

[1] Q. Zhou, M. Mirzazadeh, M. Ekici, and A. Sonmezoglu, "Analytical study of solitons in non-kerr nonlinear negative-index materials," *Nonlinear Dyn.*, vol. 86, no. 1, pp. 623–638, Oct. 2016.

[2] J. Yang, C. Huang, X. Wu, B. Sun, and X. Luo, "Dual-wavelength carpet cloak using ultrathin metasurface," *Adv. Opt. Mater.*, vol. 6, no. 14, Jul. 2018, Art. no. 1800073.

[3] M.-J. Haji-Ahmadi, V. Nayyeri, M. Soleimani, and O. M. Ramahi, "Pixelated checkerboard metasurface for ultra-wideband radar cross section reduction," *Sci. Rep.*, vol. 7, no. 1, p. 11437, Dec. 2017.

[4] H. Huang and Z. Shen, "Low-RCS reflectarray with phase controllable absorptive frequency-selective reflector," *IEEE Trans. Antennas Propag.*, vol. 67, no. 1, pp. 190–198, Jan. 2019.

[5] A. E. Minovich, A. E. Miroshnichenko, A. Y. Bykov, T. V. Murzina, D. N. Neshev, and Y. S. Kivshar, "Functional and nonlinear optical metasurfaces," *Laser Photon. Rev.*, vol. 9, no. 2, pp. 195–213, Mar. 2015.

[6] Y.-L. Xu, X.-C. Wei, and E.-P. Li, "Three-dimensional tunable frequency selective surface based on vertical graphene micro-ribbons," *J. Electromagn. Waves Appl.*, vol. 29, no. 16, pp. 2130–2138, Nov. 2015.

[7] G. Nie, Q. Shi, Z. Zhu, and J. Shi, "Selective coherent perfect absorption in metamaterials," *Appl. Phys. Lett.*, vol. 105, no. 20, Nov. 2014, Art. no. 201909.

[8] P. Rodríguez-Ulibarri, V. Pacheco-Peña, M. Navarro-Cía, A. E. Serebryannikov, and M. Beruete, "Experimental demonstration of deflection angle tuning in unidirectional fishnet metamaterials at millimeter-waves," *Appl. Phys. Lett.*, vol. 106, no. 6, Feb. 2015, Art. no. 061109.

[9] D. Samantaray and S. Bhattacharyya, "A gain-enhanced slotted patch antenna using metasurface as superstrate configuration," *IEEE Trans. Antennas Propag.*, early access, Apr. 30, 2020, doi: 10.1109/TAP.2020.2990280.

[10] A. K. Singh, M. P. Abegaonkar, and S. K. Koul, "Compact ultrathin linear graded index metasurface lens for beam steering and gain enhancement," *Int. J. RF Microw. Comput.-Aided Eng.*, vol. 30, no. 6, Jun. 2020, Art. no. e22186.

[11] I. I. Smolyaninov and V. N. Smolyaninova, "Hyperbolic metamaterials: Novel physics and applications," *Solid-State Electron.*, vol. 136, pp. 102–112, Oct. 2017.

[12] C. Zhang, J. Yang, W. Yuan, J. Zhao, J. Y. Dai, T. C. Guo, J. Liang, G. Y. Xu, Q. Cheng, and T. J. Cui, "An ultralight and thin metasurface for radar-infrared bi-stealth applications," *J. Phys. D, Appl. Phys.*, vol. 50, no. 44, Nov. 2017, Art. no. 444002.

[13] C. L. Ding, Y. B. Dong, and X. P. Zhao, "Research advances in acoustic metamaterials and metasurface," *Acta Phys. Sinica*, vol. 67, no. 19, 2018, Art. no. 194301.

[14] X. Liu, C. Meng, X. Xu, M. Tang, C. Pang, and Q. Yang, "Applications of nanostructures in wide-field, label-free super resolution microscopy," *Chin. Phys. B*, vol. 27, no. 11, Nov. 2018, Art. no. 118704.

[15] L. Shen, H. Wang, R. Li, Z. Xu, and H. Chen, "Hyperbolic-polaritons-enabled dark-field lens for sensitive detection," *Sci. Rep.*, vol. 7, no. 1, p. 6995, Dec. 2017.

[16] C.-C. Chang, W. J. M. Kort-Kamp, J. Nogan, T. S. Luk, A. K. Azad, A. J. Taylor, D. A. R. Dalvit, M. Sykora, and H.-T. Chen, "High-temperature refractory metasurfaces for solar thermophotovoltaic energy harvesting," *Nano Lett.*, vol. 18, no. 12, pp. 7665–7673, Dec. 2018.

[17] C.-S. Park, Y. C. Shin, S.-H. Jo, H. Yoon, W. Choi, B. D. Youn, and M. Kim, "Two-dimensional octagonal phononic crystals for highly dense piezoelectric energy harvesting," *Nano Energy*, vol. 57, pp. 327–337, Mar. 2019.

[18] M. Saadatzi, F. Mir, M. N. Saadatzi, and S. Banerjee, "Modeling and fabrication of a multi-axial piezoelectric energy harvester based on a metamaterial-inspired structure," *IEEE Sensors J.*, vol. 18, no. 22, pp. 9410–9419, Nov. 2018.

[19] J. Shi and A. H. Akbarzadeh, "Architected cellular piezoelectric metamaterials: Thermo-electro-mechanical properties," *Acta Mater.*, vol. 163, pp. 91–121, Jan. 2019.

[20] Z. Cohick, W. Luo, S. Perini, A. Baker, D. Wolfe, and M. Lanagan, "A novel, all-dielectric, microwave plasma generator towards development of plasma metamaterials," *Appl. Phys. Express*, vol. 9, no. 11, Nov. 2016, Art. no. 116201.

[21] D. R. Jackson, C. Caloz, and T. Itoh, "Leaky-wave antennas," *Proc. IEEE*, vol. 100, no. 7, pp. 2194–2206, Mar. 2012.

[22] O. V. Gendelman and A. F. Vakakis, "Introduction to a topical issue 'nonlinear energy transfer in dynamical and acoustical systems,'" *Phil. Trans. Roy. Soc. A, Math., Phys. Eng. Sci.*, vol. 376, no. 2127, Aug. 2018, Art. no. 20170129.

[23] C. R. Liu, J. H. Wu, K. Lu, Z. T. Zhao, and Z. Huang, "Acoustical siphon effect for reducing the thickness in membrane-type metamaterials with low-frequency broadband absorption," *Appl. Acoust.*, vol. 148, pp. 1–8, May 2019.

[24] I. Quotane, E. H. El Boudouti, and B. Djafari-Rouhani, "Trapped-mode-induced fano resonance and acoustical transparency in a one-dimensional solid-fluid phononic crystal," *Phys. Rev. B, Condens. Matter*, vol. 97, no. 2, Jan. 2018, Art. no. 024304.

[25] F. Chiadini and A. Lakhtakia, "Bicontrollable terahertz metasurface with subwavelength scattering elements of two different materials," *Appl. Opt.*, vol. 57, no. 2, p. 189, Jan. 2018.

[26] X. Luo, "Subwavelength optical engineering with metasurface waves," *Adv. Opt. Mater.*, vol. 6, no. 7, Apr. 2018, Art. no. 1701201.

[27] Y. Wang, L. Wang, L. Dong, S. Liu, J. Wang, Y. Leng, and Y. Sun, "Design of multifunctional metamaterial absorber based on electro-optic properties of graphene," *Scientia Sinica Phys., Mechanica Astronomica*, vol. 48, no. 4, Apr. 2018, Art. no. 047001.

[28] J. Liang, X. Song, J. Li, K. Lan, and P. Li, "A visible-near infrared wavelength-tunable metamaterial absorber based on the structure of au triangle arrays embedded in VO2 thin film," *J. Alloys Compounds*, vol. 708, pp. 999–1007, Jun. 2017.

[29] Y. Zhang, J. Duan, B. Zhang, W. Zhang, and W. Wang, "A flexible metamaterial absorber with four bands and two resonators," *J. Alloys Compounds*, vol. 705, pp. 262–268, May 2017.

[30] D.-E. Wen, X. Huang, P. Ren, Q. Zhang, X. Huang, and W. Hui, "Study on the properties of the two-dimensional curved surface metamaterial," *AEU Int. J. Electron. Commun.*, vol. 83, pp. 376–397, Jan. 2018.

[31] Z. Yang, F. Luo, W. Zhou, D. Zhu, and Z. Huang, "Design of a broadband electromagnetic absorbers based on TiO2/Al2O3 ceramic coatings with metamaterial surfaces," *J. Alloys Compounds*, vol. 687, pp. 384–388, Dec. 2016.

[32] X. Liu, K. Fan, I. V. Shadrivov, and W. J. Padilla, "Experimental realization of a terahertz all-dielectric metasurface absorber," *Opt. Express*, vol. 25, no. 1, p. 191, Jan. 2017.

[33] M. Bakır, M. Karaaslan, E. Unal, O. Akgol, and C. Sabah, "Microwave metamaterial absorber for sensing applications," *Opto-Electron. Rev.*, vol. 25, no. 4, pp. 318–325, Dec. 2017.

[34] J. Cui, B. Zhang, H. Xu, H. Sun, and G. Shao, "Topological flexible metamaterials with isotropic dual-frequency terahertz-band absorption," *Opt. Commun.*, vol. 441, pp. 90–95, Jun. 2019.

[35] D. Wu, C. Liu, Y. Liu, L. Yu, Z. Yu, L. Chen, R. Ma, and H. Ye, "Numerical study of an ultra-broadband near-perfect solar absorber in the visible and near-infrared region," *Opt. Lett.*, vol. 42, no. 3, p. 450, Feb. 2017.

[36] P. Rufangura and C. Sabah, "Wide-band polarization independent perfect metamaterial absorber based on concentric rings topology for solar cells application," *J. Alloys Compounds*, vol. 680, pp. 473–479, Sep. 2016.

[37] P. Rufangura and C. Sabah, "Design and characterization of a dual-band perfect metamaterial absorber for solar cell applications," *J. Alloys Compounds*, vol. 671, pp. 43–50, Jun. 2016.

[38] D. Shin, G. Kang, P. Gupta, S. Behera, H. Lee, A. M. Urbas, W. Park, and K. Kim, "Thermoplasmonic and photothermal metamaterials for solar energy applications," *Adv. Opt. Mater.*, vol. 6, no. 18, Sep. 2018, Art. no. 1800317.

[39] M. Shahidul Islam, M. Samsuzzaman, G. K. Beng, N. Misran, N. Amin, and M. T. Islam, "A gap coupled hexagonal split ring resonator based metamaterial for S-band and X-band microwave applications," *IEEE Access*, vol. 8, pp. 68239–68253, 2020.

[40] I. E. Khodasevych, L. Wang, A. Mitchell, and G. Rosengarten, "Micro- and nanostructured surfaces for selective solar absorption," *Adv. Opt. Mater.*, vol. 3, no. 7, pp. 852–881, Jul. 2015.

[41] S. S. Islam, M. R. Iqbal Faruque, and M. T. Islam, "A dual-polarized metamaterial-based cloak," *Mater. Res. Bull.*, vol. 96, pp. 250–253, Dec. 2017.

[42] D. Hu, H.-Y. Wang, and Q.-F. Zhu, "Design of six-band terahertz perfect absorber using a simple U-Shaped closed-ring resonator," *IEEE Photon. J.*, vol. 8, no. 2, pp. 1–8, Apr. 2016.

[43] J. Yang, Z. Zhu, J. Zhang, C. Guo, W. Xu, K. Liu, X. Yuan, and S. Qin, "Broadband terahertz absorber based on multi-band continuous plasmon resonances in geometrically gradient dielectric-loaded graphene plasmon structure," *Sci. Rep.*, vol. 8, no. 1, p. 3239, Dec. 2018.

[44] X. Yan, T. Wang, S. Xiao, T. Liu, H. Hou, L. Cheng, and X. Jiang, "Dynamically controllable plasmon induced transparency based on hybrid metal-graphene metamaterials," *Sci. Rep.*, vol. 7, no. 1, Dec. 2017, Art. no. 13917.

[45] M. Liu, M. Susli, D. Silva, G. Putrino, H. Kala, S. Fan, M. Cole, L. Faraone, V. P. Wallace, W. J. Padilla, D. A. Powell, I. V. Shadrivov, and M. Martyniuk, "Ultrathin tunable terahertz absorber based on MEMS-driven metamaterial," *Microsyst. Nanoeng.*, vol. 3, no. 1, pp. 1–6, Dec. 2017.

[46] C. L. Holloway, E. F. Kuester, and A. Dienstfrey, "Characterizing metasurfaces/metafilms: The connection between surface susceptibilities and effective material properties," *IEEE Antennas Wireless Propag. Lett.*, vol. 10, pp. 1507–1511, 2011.

[47] S. Bhattacharyya and K. V. Srivastava, "Triple band polarization-independent ultra-thin metamaterial absorber using electric field-driven LC resonator," *J. Appl. Phys.*, vol. 115, no. 6, Feb. 2014, Art. no. 064508.

[48] R. Yahiaoui and H. H. Ouslimani, "Broadband polarization-independent wide-angle and reconfigurable phase transition hybrid metamaterial absorber," *J. Appl. Phys.*, vol. 122, no. 9, Sep. 2017, Art. no. 093104.

[49] T. T. Nguyen and S. Lim, "Design of metamaterial absorber using eight-resistive-arm cell for simultaneous broadband and wide-incidence-angle absorption," *Sci. Rep.*, vol. 8, no. 1, p. 6633, Dec. 2018.

[50] W. Chen, R. Chen, Y. Zhou, and Y. Ma, "Broadband metamaterial absorber with an in-band metasurface function," *Opt. Lett.*, vol. 44, no. 5, p. 1076, Mar. 2019.

[51] G. Haitao, W. Jianjiang, X. Baocai, L. Ze, and S. Qingtao, "Broadband metamaterial absorber based on magnetic substrate and resistance rings," *Mater. Res. Express*, vol. 6, no. 4, Jan. 2019, Art. no. 045803.

[52] C. M. Tran, H. Van Pham, H. T. Nguyen, T. T. Nguyen, L. D. Vu, and T. H. Do, "Creating multiband and broadband metamaterial absorber by multiporous square layer structure," *Plasmonics*, vol. 14, no. 6, pp. 1587–1592, Dec. 2019.

[53] T. Q. H. Nguyen, T. K. T. Nguyen, T. N. Cao, H. Nguyen, and L. G. Bach, "Numerical study of a broadband metamaterial absorber using a single split circle ring and lumped resistors for X-band applications," *AIP Adv.*, vol. 10, no. 3, Mar. 2020, Art. no. 035326.

JUNPING DUAN received the Ph.D. degree from the North University of China in 2015. She is a Professor with the North University of China. She has mastered a project through the National Natural Science Foundation of China and the National Defense Pre-Research Foundation of China. Her research interests include flexible antennas, THz filters, metamaterials, and waveguide slot array antennas.

RUI LIU was born in Lüliang, China. He received the B.S. degree in measurement and control technology and instrumentation from Beijing Normal University, Zhuhai, in 2018. He is currently pursuing the M.S. degree with the North University of China. His research interests include end-fire antennas, metamaterials, absorbers, and MEMS technology.

HONGCHENG XU was born in Huanggang, China. He received the B.S. degree in detection guidance and control technology, and the M.S. degree in instrument science and technology from the North University of China, in 2016 and 2019, respectively. He is currently pursuing the Ph.D. degree with Xidian University. His research interests include flexible antennas, conformal antennas, 5G antennas, electromagnetic metamaterials, and MEMS technology.

RUI ZHANG was born in Jiamusi, China. She received the B.S. degree in measurement and control technology and instrumentation from the North University of China, in 2018, where she is currently pursuing the M.S. degree. Her research interests include flexible antennas, 5G antennas, and MEMS technologies.

BINZHEN ZHANG is currently a Professor with the North University of China, China. He is also the Deputy Director of the Key Laboratory of Instrumentation Science and Dynamic Measurement, Ministry of Education, North University of China. He has more than 100 published articles in the SCI library. His remarkable scientific work has contributed to great progress in the academic world. His research interests include functional materials, nano-materials, MEMS, and RF and microwave technology, including antennas, filters, couplers, power dividers, phase shifters, and amplifiers.

BYUNG-SUNG KIM (Member, IEEE) received the B.S., M.S., and Ph.D. degrees in electronics engineering from Seoul National University, Seoul, South Korea, in 1989, 1991, and 1997, respectively. In 1997, he joined the College of Information and Communication Engineering, Sungkyunkwan University, Suwon, South Korea, where he is currently a Professor. In 2013, he was a Visiting Researcher with the University of California at Santa Barbara. His research interests include high-frequency device modeling and RF/millimeter-wave CMOS integrated circuit design.

• • •